Computers and Fluids 275 (2024) 106252

Contents lists available at ScienceDirect

Computers and Fluids

journal homepage: www.elsevier.com/locate/compfluid

Investigation and assessment of production- and dissipation-limited DDES methods for rocket combustion chamber simulations

Timo Seitz [a,*], Peter Gerlinger [a,b]

[a] Institute of Combustion Technology, German Aerospace Center (DLR), Pfaffenwaldring 38-40, Stuttgart, 70569, Germany
[b] Institute of Combustion Technology for Aerospace Engineering (IVLR), University of Stuttgart, Pfaffenwaldring 38-40, Stuttgart, 70569, Germany

ARTICLE INFO

Keywords:
Turbulence modeling
Hybrid RANS/LES model
iDDES
l^2-ω-DDES
Rocket combustion chamber

ABSTRACT

This paper compares two different delayed detached-eddy simulation (DDES) techniques, namely iDDES and l^2-ω-DDES. Their performance is investigated with and without combustion. While iDDES limits the dissipation term of the turbulent kinetic energy equation, l^2-ω-DDES confines its production term. In this way, both models achieve that resolved turbulence is enhanced in regions of separated flow. On the other hand, the models show significant differences. In a first step this is investigated using three non-reactive test cases. While here the first-order moments are in a fairly good agreement, the second-order moments exhibit slight differences. Despite the similarities in first- and second-order moments, the instantaneous flow fields differ considerably with the iDDES displaying finer vortex structures. This is caused by different levels of eddy viscosity. These disparities are even more pronounced in case of a laboratory-scale rocket combustion chamber, where strong differences in quantities as the wall heat flux are observed. This clearly demonstrates an impact on the combustion process.

1. Introduction

In the development of rocket combustion chambers, the demand for time-resolved, high-fidelity turbulence models is rising. They should be able to capture all relevant physical processes such as the wall heat flux, pressure fluctuations or the flow field correctly. Due to the inherently unsteady nature of the flow in rocket combustors, Reynolds-averaged Navier-Stokes (RANS) simulations often fail to obtain a convergent solution on fine grids [1,2]. On the other hand, wall-resolved large-eddy simulation (LES) or even direct numerical simulation (DNS) of rocket combustion chambers are hardly possible to date.

Hybrid RANS/LES methods offer a good tradeoff between accuracy and computational effort. Numerous strategies exist for combining RANS and LES, see e.g. [3–5] for an overview on various hybrid methods. One of the most popular approaches is the detached-eddy simulation (DES) of Spalart et al. [6]. The basic idea is to use a length-scale l_{DES} in order to switch between RANS and LES. The original DES formulation was based on the Spalart–Allmaras turbulence model [6]. Thus, no modification of the underlying transport equation is required as a lengthscale is already intrinsically used in this model. Strelets [7] extended this approach to two-equation models. Again, a lengthscale is used to modify the dissipation term in the equation of the turbulent kinetic energy k. An increased dissipation of k in free shear layers in comparison to RANS mode enhances the share of resolved turbulence in that region. DES suffers from various drawbacks, which have been fixed over time by additional functions and constants, increasing the complexity of the model. Unphysical grid-induced separation (GIS) [8] is caused by a wrong dependence on grid spacing and aspect ratio. In addition, Nikitin et al. [9] noticed two separate log-layers in turbulent channel flows that are shifted by several units of the non-dimensional velocity. This issue is called log-layer mismatch (LLM). In order to overcome these issues, several improvements have been proposed. The introduction of a shielding function resolves GIS. The resulting model is termed delayed detached-eddy simulation (DDES) [10]. In order to alleviate LLM, Shur et al. [11] modified the definition of the lengthscale and introduced a number of additional empirical functions. This iDDES is very popular and one of the models studied in this work.

Apart from a modification of the dissipation term, it is also possible to alter the production term of the k-equation. This is the concept of the second hybrid RANS/LES method investigated in this paper, called l^2-ω-DDES [12]. An adjusted lengthscale is applied in order to ameliorate LLM. The great advantage of the l^2-ω-DDES is its simplicity. Compared with iDDES, less empirical functions and constants are required. This simplifies the implementation in the code and it is easier to keep track of which function is active in case of complex geometries or flow conditions. In addition to basic test cases, typical applications of the l^2-ω-DDES are diffusors [13,14] and transition investigations [14,15].

The l^2-ω-DDES is still relatively unknown and will be compared in this paper with the more frequently employed iDDES. It will be shown

* Corresponding author.
E-mail address: timo.seitz@dlr.de (T. Seitz).

https://doi.org/10.1016/j.compfluid.2024.106252
Received 22 December 2023; Received in revised form 13 March 2024; Accepted 25 March 2024
Available online 27 March 2024

that the different formulations cause differences in the flow quantities. In a first step, simple, non-reactive validation test cases are used to identify the general behavior of the corresponding DDES method. Many of these standard problems, such as attached and separated boundary layers, recirculation zones and mixing layers, are part of the flow field in the subscale rocket combustion chamber which is investigated next. It will be shown that the differences between both models are enhanced in case of a high pressure combustor. Moreover, a quick and correct transfer to LES downstream of the coaxial injector is extremely important for rocket combustion chamber simulations. It will be shown that the type of the DDES model in use has a strong impact on turbulent mixing, combustion and even the wall heat flux of the model rocket combustor.

2. Numerical methodology

All simulations are performed with the in-house code TASCOM3D (Turbulent All Speed Combustion Multigrid 3D), which has been developed and successfully applied to a wide range of non-reacting and reacting flows in both the subsonic and the supersonic regime, e.g. [16–22]. The following subsections briefly describe the underlying equations as well as the applied numerical methods.

2.1. Governing equations

Turbulent combustion is described by the compressible Navier–Stokes equations that additionally include transport equations for turbulence modeling, species transport and turbulence-chemistry interaction (TCI). The unsteady filtered set of equations is given by

$$\frac{\partial \mathbf{Q}}{\partial t} + \frac{\partial \left(\mathbf{F} - \mathbf{F}_v\right)}{\partial x} + \frac{\partial \left(\mathbf{G} - \mathbf{G}_v\right)}{\partial y} + \frac{\partial \left(\mathbf{H} - \mathbf{H}_v\right)}{\partial z} = \mathbf{S} \tag{1}$$

with the vector of conservative quantities

$$\mathbf{Q} = \left[\bar{\rho}, \bar{\rho}\tilde{u}, \bar{\rho}\tilde{v}, \bar{\rho}\tilde{w}, \bar{\rho}\tilde{E}, \bar{\rho}k, \bar{\rho}\omega, \bar{\rho}\sigma_T, \bar{\rho}\sigma_Y, \bar{\rho}\tilde{Y}_i\right]^\top,\ i = 1, \ldots, N_k - 1\ . \tag{2}$$

$\mathbf{Q}$ consists of the spatially Reynolds-filtered density $\bar{\rho}$, the Favre-filtered velocities $\tilde{u}$, $\tilde{v}$, $\tilde{w}$ in each coordinate direction, the total specific energy $\tilde{E}$, the turbulence quantities k and ω, the subgrid temperature variance σ_T, the sum of subgrid variances of the species mass fractions σ_Y as well as the $N_k - 1$ independent species mass fractions $\tilde{Y}_i$. N_k denotes the number of considered species. For better readability the overbars $\bar{(\cdot)}$ and $\tilde{(\cdot)}$ are omitted in what follows. $\mathbf{F}$, $\mathbf{G}$ and $\mathbf{H}$ indicate the inviscid flux vectors in x-, y- and z-direction, respectively, while $\mathbf{F}_v$, $\mathbf{G}_v$ and $\mathbf{H}_v$ are the corresponding viscous vectors. The source term vector includes only terms resulting from turbulence and chemistry modeling and is given by

$$\mathbf{S} = \left[0, 0, 0, 0, 0, S_k, S_\omega, S_{\sigma_T}, S_{\sigma_Y}, S_{Y_i}\right]^\top,\ i = 1, \ldots, N_k - 1\ . \tag{3}$$

In order to close this set of equations, the ideal gas law is used.

2.2. Numerical solver

The set of equations given above is discretized with a cell-centered finite-volume method based on block-structured grids. It is solved using a fully implicit lower–upper symmetric Gauss–Seidel algorithm [23–25]. Time-accurate simulations utilize a second order backward differentiation formula (BDF) scheme [26] in time where the non-linear set of equations is solved by a dual time-stepping scheme with a couple of inner Newton iterations [27].

The inviscid fluxes are calculated with an AUSM$^+$-up [28] flux-vector splitting scheme. In this method, the primitive values at the cell-interfaces are required, which are reconstructed from the available cell averages. For LES, it is important to keep the numerical dissipation low. Thus, a high-order discretization, which is a blend between an unlimited sixth order central and a limited fifth order upwind-biased discretization, is applied. In the latter case, the multi-dimensional limiting process with low dissipation (MLP$^{\text{ld}}$) [2,19] is employed to ensure the total variation diminishing (TVD) criterion [29]. The viscous fluxes are discretized with a central discretization. The hybrid RANS/LES approaches, namely iDDES and l^2-ω-DDES, are presented in detail in Section 3.

For hydrogen-oxygen combustion, finite-rate chemistry is applied based on the kinetic reaction mechanism of Ó Conaire [30]. This kinetic scheme consists of eight species and 19 chemical reactions and is validated for high pressures as in the present rocket model combustor. To consider subgrid TCI, an assumed probability density function (APDF) approach [31–34] is utilized. Assuming statistical independence of temperature and species fluctuations, the joint pdf is described by a clipped Gaussian distribution for temperature [35] and a multi-variate β-distribution [31,36] for the species mass fractions. Therefore, two additional transport equations for the subgrid temperature variance σ_T and the sum of all species mass fraction variances σ_Y need to be solved, see Eq. (2).

3. Hybrid RANS/LES models

Both hybrid RANS/LES methods applied in this work are based on the k-ω turbulence model of Wilcox [37,38]. The governing equations for the turbulent kinetic energy k and the specific dissipation rate ω in its basic form [37] are given as

$$\frac{\mathrm{D}(\rho k)}{\mathrm{D}t} = 2\mu_t \left|\bar{\mathbf{S}}\right|^2 - \frac{2}{3}\rho k \nabla\cdot\mathbf{u} - \beta_k \rho k\omega + \nabla\cdot\left[\left(\mu_l + \sigma_k \rho k/\omega\right)\nabla k\right] \tag{4}$$

$$\frac{\mathrm{D}(\rho \omega)}{\mathrm{D}t} = \alpha\left(2\rho\left|\bar{\mathbf{S}}\right|^2 - \frac{2}{3}\rho\omega\nabla\cdot\mathbf{u}\right) - \beta_\omega \rho\omega^2 + \nabla\cdot\left[\left(\mu_l + \sigma_\omega \rho k/\omega\right)\nabla\omega\right]. \tag{5}$$

Herein, μ_l and $\mu_t = \rho\, k/\omega$ denote the molecular and the turbulent viscosity, respectively. The term $\left|\bar{\mathbf{S}}\right|$ is the magnitude of the traceless mean strain-rate tensor

$$\bar{\mathbf{S}} = \frac{1}{2}\left(\nabla\mathbf{u} + (\nabla\mathbf{u})^\top\right) - \frac{1}{3}\left(\nabla\cdot\mathbf{u}\right)\mathbf{I} \tag{6}$$

and $\alpha = 5/9$, $\beta_k = 0.09$, $\beta_\omega = 0.075$, $\sigma_k = 0.5$ and $\sigma_\omega = 0.5$ are constants. In DDES-type models, these equations are modified in a way to resolve most of the turbulent scales in free shear layers. This is done by the introduction of a DDES lengthscale l_{DDES} that determines whether RANS or LES mode is active. There exist various possibilities to switch from RANS to LES, which, in addition to some other modifications, lead to different models. As will be shown later, differences not only occur in the transition zone from RANS to LES but also in the LES mode.

3.1. iDDES

Shur et al. [11] developed iDDES in order to alleviate the issue of LLM and to allow the model to act as a wall-modeled LES (WMLES) in case of sufficiently fine grids and turbulence transported from upstream. Originally, iDDES was based on the Spalart–Allmaras or the k-ω SST RANS model [11,39] and has since been used primarily with these two models, even if versions based on a k-ϵ [40] or a Reynolds-stress model [41] have been published, too. The iDDES method in this work uses the k-ω model [38] as background RANS model. Identical to DDES, a lower limit is placed on the dissipation term of the turbulent kinetic energy equation

$$\frac{\mathrm{D}(\rho k)}{\mathrm{D}t} = 2\mu_t \left|\bar{\mathbf{S}}\right|^2 - \frac{2}{3}\rho k \nabla\cdot\mathbf{u} - \frac{\rho k^{3/2}}{l_{\text{iDDES}}} + \nabla\cdot\left[\left(\mu_l + \sigma_k \rho k/\omega\right)\nabla k\right] \tag{7}$$

by using the lengthscale l_{iDDES}. The iDDES lengthscale switches between the individual lengthscales of the RANS and LES modes what requires a number of empirical functions. The lengthscales are given by

$$l_{\text{iDDES}} = \tilde{f}_{\text{d}}\left(1 + f_{\text{e}}\right) l_{\text{RANS}} + \left(1 - \tilde{f}_{\text{d}}\right) l_{\text{LES}} \tag{8}$$

$$l_{\text{RANS}} = \frac{\sqrt{k}}{\beta_k \omega} \tag{9}$$

$$l_{\mathrm{LES}} = C_{\mathrm{DES}}\Delta \tag{10}$$

$$\Delta = \min\left[\max\left(0.15d_{\mathrm{w}}, 0.15h_{\max}, h_{\mathrm{wn}}\right), h_{\max}\right], \tag{11}$$

where d_{w} is the distance to the wall, h_{wn} denotes the grid step in wall-normal direction and $h_{\max}$ is the maximum local grid spacing [11]. The value of C_{DES} is set to $C_{\mathrm{DES}} = 0.2$. The lengthscale l_{iDDES} is used to switch between RANS and LES mode and the different branches of iDDES, namely the DDES and the WMLES branch, can be activated as well. The basis for this behavior are the empirical shielding function $\tilde{f}_{\mathrm{d}}$ and the elevating function f_{e}. The shielding function reads

$$\tilde{f}_{\mathrm{d}} = \max\left\{1 - f_{\mathrm{d}}, f_{\mathrm{b}}\right\} \tag{12}$$

with

$$f_{\mathrm{d}} = 1 - \tanh\left[\left(20r_{\mathrm{d}}\right)^3\right] \quad \text{and} \tag{13}$$

$$f_{\mathrm{b}} = \min\left\{2\exp\left(-9\alpha^2\right), 1.0\right\}. \tag{14}$$

Together with the elevating function defined below, f_{b} is added to incorporate the WMLES capabilities while f_{d} represents the DDES branch. Here, the function r_{d} is

$$r_{\mathrm{d}} = \frac{\mu_t/\rho + \nu}{\kappa^2 d_{\mathrm{w}}^2 \max\left\{\sqrt{\nabla\mathbf{u}:\nabla\mathbf{u}}, 10^{-19}\right\}}, \tag{15}$$

where the von Karman constant is set to $\kappa = 0.41$. The empirical function α solely depends on geometry and grid spacing and is defined as

$$\alpha = 0.25 - d_{\mathrm{w}}/h_{\max}. \tag{16}$$

The elevating function is given as

$$f_{\mathrm{e}} = \max\left\{f_{\mathrm{e1}} - 1, 0\right\} f_{\mathrm{e2}} \tag{17}$$

with

$$f_{\mathrm{e1}} = \begin{cases} 2\exp\left\{-9\alpha^2\right\} & \text{if } \alpha < 0 \\ 2\exp\left\{-11\alpha^2\right\} & \text{if } \alpha \geq 0 \end{cases} \quad \text{and} \tag{18}$$

$$f_{\mathrm{e2}} = 1 - \max\left\{f_{\mathrm{t}}, f_{\mathrm{l}}\right\}, \tag{19}$$

respectively and the functions f_{t} and f_{l} are

$$f_{\mathrm{t}} = \tanh\left[\left(c_{\mathrm{t}}^2 r_{\mathrm{dt}}\right)\right] \quad \text{with} \quad r_{\mathrm{dt}} = \frac{\mu_t/\rho}{\kappa^2 d_{\mathrm{w}}^2 \max\left\{\sqrt{\nabla\mathbf{u}:\nabla\mathbf{u}}, 10^{-19}\right\}}, \tag{20}$$

$$f_{\mathrm{l}} = \tanh\left[\left(c_{\mathrm{l}}^2 r_{\mathrm{dl}}\right)\right] \quad \text{with} \quad r_{\mathrm{dl}} = \frac{\nu}{\kappa^2 d_{\mathrm{w}}^2 \max\left\{\sqrt{\nabla\mathbf{u}:\nabla\mathbf{u}}, 10^{-19}\right\}}. \tag{21}$$

Especially the elevating function, which only acts on l_{RANS}, plays a crucial role in mitigating LLM [11]. The values of c_{t} and c_{l} depend on the background RANS model. Furthermore, the applied numerical solver has an influence on LLM [42]. For these reasons, literature values are not used, but instead the constants of the elevating function are calibrated based on validation simulations. The chosen values are $c_{\mathrm{t}} = 1.0$ and $c_{\mathrm{l}} = 1.0$.

As the iDDES used here is based on a new version of the k-ω model [38], a cross-diffusion term is added to the ω-equation

$$\frac{\mathrm{D}(\rho\omega)}{\mathrm{D}t} = \alpha\left(2\rho\left|\bar{\mathbf{S}}\right|^2 - \frac{2}{3}\rho\omega\nabla\cdot\mathbf{u}\right) - \beta_\omega\rho\omega^2 + \nabla\cdot\left[\left(\mu_l + \sigma_\omega\rho k/\omega\right)\nabla\omega\right] + \sigma_d\frac{\rho}{\omega}\nabla k\cdot\nabla\omega. \tag{22}$$

with

$$\sigma_d = \begin{cases} 0 & \text{if } \nabla k\cdot\nabla\omega \leq 0 \\ \sigma_{d0} & \text{if } \nabla k\cdot\nabla\omega > 0, \end{cases} \qquad \sigma_{d0} = 0.125. \tag{23}$$

In addition, the model constants are slightly adapted and the values given by Wilcox [38] are used. These read as $\alpha = 0.52$, $\beta_k = 0.09$, $\beta_\omega = \beta_0 f_\beta$, $\beta_0 = 0.0708$, $\sigma_k = 0.6$ and $\sigma_\omega = 0.5$. Here, f_β is a flow-dependent quantity. For brevity, its definition is not given, but instead the reader is referred to Wilcox [38]. The turbulent viscosity is calculated as

$$\mu_t = \frac{\rho k}{\tilde{\omega}}, \tag{24}$$

with the effective specific dissipation rate [38]

$$\tilde{\omega} = \max\left\{\omega, 0.875\sqrt{\frac{2\left|\bar{\mathbf{S}}\right|^2}{\beta_k}}\right\}. \tag{25}$$

Please note that the influence of this stress-limiter modification is negligible in LES mode, but becomes relevant in RANS mode.

3.2. l^2-ω-DDES

Another DDES-type model was recently formulated by Reddy et al. [12] and termed l^2-ω-DDES. It also uses the k-ω model [37] as background RANS model. Here, the turbulent kinetic energy equation is modified by placing an upper limit on the production term by introducing the lengthscale l_{DDES}

$$\frac{\mathrm{D}(\rho k)}{\mathrm{D}t} = 2\rho l_{\mathrm{DDES}}^2\omega\left|\bar{\mathbf{S}}\right|^2 - \frac{2}{3}\rho k\nabla\cdot\mathbf{u} - \beta_k\rho k\omega + \nabla\cdot\left[\left(\mu_l + \sigma_k\rho k/\omega\right)\nabla k\right]. \tag{26}$$

The transport equation for ω remains unaltered (see Eq. (5)). In addition, the constants of Eqs. (26) and (5) are chosen according to Wilcox [37] as given in Section 3. The lengthscale definitions differ from iDDES and are given as

$$l_{\mathrm{DDES}} = l_{\mathrm{RANS}} - f_{\mathrm{d}}\max\left(0, l_{\mathrm{RANS}} - l_{\mathrm{LES}}\right) \tag{27}$$

$$l_{\mathrm{RANS}} = \frac{\sqrt{k}}{\omega} \tag{28}$$

$$l_{\mathrm{LES}} = C_{\mathrm{DES}}\Delta \quad \text{with} \quad \Delta = f_{\mathrm{d}}V^{1/3} + (1 - f_{\mathrm{d}})h_{\max}. \tag{29}$$

The value of C_{DES} is constant and set to $C_{\mathrm{DES}} = 0.12$ [12]. Please note that, in contrast to Eq. (9), the constant β_ω is not included in the definition of l_{RANS}. The shielding function f_d is calculated from

$$f_{\mathrm{d}} = 1 - \tanh\left[\left(8r_{\mathrm{d}}\right)^3\right] \quad \text{with} \quad r_{\mathrm{d}} = \frac{k/\omega + \nu}{\kappa^2 d_{\mathrm{w}}^2 \max\left\{\sqrt{\nabla\mathbf{u}:\nabla\mathbf{u}}, 10^{-19}\right\}}. \tag{30}$$

Due to stability issues, a spatial uniformization of the velocity gradient according to He et al. [43] is applied. The calculation of μ_t is based on a Smagorinsky-type formulation

$$\mu_t = \rho l_{\mathrm{DDES}}^2\omega, \tag{31}$$

which, compared to iDDES, is independent of k. Due to this expression, the equation for the turbulent kinetic energy loses its significance in the LES mode as k no longer enters directly into μ_t, but only indirectly via the ω-equation. This approach facilitates the dynamic computation of the model constant C_{DES} [13,15]. However, for a better comparison with iDDES, a constant value for C_{DES} is adopted in this paper.

Both presented hybrid RANS/LES models are DDES-type models. Nevertheless, some significant differences arise. The main difference between iDDES and l^2-ω-DDES is the fact that the former is dissipation-limited, while the latter is production-limited. In both cases, the aim is to enhance turbulence in the eddying regions. One disadvantage of the iDDES, which is not present in the l^2-ω-DDES, is the extensive use of empirical functions [11].

3.3. Investigation of the subgrid formulation at equilibrium conditions

One condition often placed on hybrid RANS/LES methods is that these models should transition to a Smagorinsky-like model in LES mode at local equilibrium conditions [7]. This means that the turbulent viscosity is expressed as

$$\mu_t = \rho\left(C_S\Delta\right)^2\sqrt{2\left|\bar{\mathbf{S}}\right|^2} \tag{32}$$

and thus is proportional to both the square of the LES filter width and the magnitude of the mean strain-rate tensor. To investigate LES equilibrium conditions of the DDES models, equilibrium between the production and the dissipation terms of the turbulence equations is assumed. Accordingly, all transport terms are dropped. Due to the different formulations of the applied models they strongly differ at equilibrium conditions. This will be shown in a short analysis. For simplicity, the compressibility terms occurring in the turbulence equations are omitted.

3.3.1. iDDES

Disregarding the cross-diffusion term as its influence is negligible in LES mode, the local equilibrium expressions for ω and k can be derived as

$$\omega^{\mathrm{eq}} = \sqrt{\frac{\alpha}{\beta_\omega}}\sqrt{2\left|\bar{\mathbf{S}}\right|^2}, \quad k^{\mathrm{eq}} = 2\left(C_{\mathrm{DES}}\Delta\right)^2 \frac{\beta_\omega}{\alpha}\left|\bar{\mathbf{S}}\right|^2. \tag{33}$$

It is worth noting that k^{eq} adopts a form that is similar to expressions typically used to model the turbulent kinetic energy in (weakly) compressible flows [44,45]. Combining the coefficients (i.e. $2\frac{\beta_\omega}{\alpha}C_{\mathrm{DES}}^2$) returns a value of approximately 0.01, which is slightly higher than the value 0.0066 used by Speziale et al. [45], but significantly lower than the value of 0.17 utilized by Yoshizawa [44]. Inserting Eq. (33) into Eq. (24) results in

$$\mu_t^{\mathrm{eq}} = \rho\left(C_{\mathrm{DES}}\Delta\right)^2\left(\frac{\beta_\omega}{\alpha}\right)^{3/2}\sqrt{2\left|\bar{\mathbf{S}}\right|^2}. \tag{34}$$

Thus, in case of local equilibrium conditions, the iDDES reduces to a Smagorinsky-like subgrid-scale model. For this to be valid, local equilibrium has to be reached for both k and ω simultaneously. According to Kok et al. [46] and Yan et al. [47], however, this is unlikely to occur in practical problems, since the source terms of the turbulence equations in LES mode are not modeled consistently [46]. If Eq. (34) is brought in an identical form as the Smagorinsky eddy viscosity from Eq. (32), the corresponding modeling constant obtained from C_{DES}, β_ω and α is approximately four times smaller than the Smagorinsky constant $C_s = 0.18$. Accordingly, the values of the turbulent viscosity of the iDDES at local equilibrium conditions are lower by a factor of more than 15 compared to the Smagorinsky model.

3.3.2. l^2-ω-DDES

The same analysis is performed for the l^2-ω-DDES as well. Equating the production and the dissipation terms of the k- and ω-equations yields

$$\omega^{\mathrm{eq}} = \sqrt{\frac{\alpha}{\beta_\omega}}\sqrt{2\left|\bar{\mathbf{S}}\right|^2}, \quad k^{\mathrm{eq}} = 2\left(C_{\mathrm{DES}}\Delta\right)^2 \frac{1}{\beta_k}\left|\bar{\mathbf{S}}\right|^2. \tag{35}$$

As can be seen, the formulations for ω^{eq} are identical for both iDDES and l^2-ω-DDES. The expressions for k^{eq} are similar, too. However, the prefactors differ. Comparison with the iDDES shows that k^{eq} of the l^2-ω-DDES is higher by a factor of approximately 30. Using ω^{eq}, Eq. (31) becomes

$$\mu_t^{\mathrm{eq}} = \rho\left(C_{\mathrm{DES}}\Delta\right)^2\sqrt{\frac{\alpha}{\beta_\omega}}\sqrt{2\left|\bar{\mathbf{S}}\right|^2}. \tag{36}$$

In contrast to the iDDES, local equilibrium has to be assumed for ω only, whereas k^{eq} is not used in the calculation of μ_t^{eq}. It is worth noting that the derivation of C_{DES} in the l^2-ω-DDES formulation is based on the local equilibrium assumption and a subsequent comparison with the Smagorinsky constant, for which Reddy et al. [12] use a value of $C_s = 0.2$. Thus, the l^2-ω-DDES at equilibrium conditions exactly corresponds to a Smagorinsky model, including the modeling constant. This is in contrast to the iDDES which becomes a Smagorinsky-like subgrid model however with a μ_t which is more than 15 times smaller than for the l^2-ω-DDES. On the other hand, the LES filter width Δ of the iDDES is higher than the one of the l^2-ω-DDES for typical DDES cases. This slightly reduces the difference between both models. Nonetheless, it has to be highlighted that the turbulent viscosities obtained for the l^2-ω-DDES are significantly higher than those of the iDDES.

4. Non-reactive test cases

In this section, three different non-reactive test cases are presented. The first one, the so-called decaying isotropic homogeneous turbulence (DIHT), is a widely simulated case to demonstrate the scale-resolving properties of hybrid RANS/LES models. The other two test cases are wall-bounded flows, namely a turbulent channel and a backward-facing step (BFS).

4.1. Decaying isotropic homogeneous turbulence (DIHT)

The conditions for the DIHT test case correspond to the experiment of Comte-Bellot and Corrsin [48]. The numerical domain is cubic with periodic boundary conditions in all directions. Hybrid RANS/LES simulations are performed on two isotopic grids with 64^3 and 128^3 volumes, respectively. The initial velocity field originates from filtered DNS data from Wray [49]. Both, the experimental and the DNS data are used for comparison.

In order to determine the initial turbulence field, Bunge et al. [50] suggested to perform a preceding steady-state simulation with frozen velocity fields. However, this method was not applicable for the l^2-ω-DDES as it does not converge to a physically valid field. Instead, the initial values are determined using Eqs. (33) and (35), respectively.

For this test case, both iDDES and l^2-ω-DDES operate exclusively in LES mode. Nevertheless, differences arise as the turbulent viscosity is calculated differently. Fig. 1(a) compares the energy spectra of both simulations on the different grids at a non-dimensional time of $t^* = 42$ as defined in [48]. This corresponds to a Taylor microscale Reynolds number of $Re_\lambda = 71.5$ in the DNS [49]. For small wavenumbers, iDDES and l^2-ω-DDES nearly coincide independent of the mesh size. However, for wavenumbers close to the cutoff wavenumber, iDDES shows a slight increase in energy, especially for the grid with 64^3 volumes. This indicates that the model does not provide enough subgrid dissipation in this case. The observed behavior can be explained with the initial flow fields of k and ω. When using another method to generate the initial fields for k and ω, e.g. the method described in [50], this energy accumulation is less pronounced due to higher levels of k and thus higher turbulent viscosities at the beginning. The l^2-ω-DDES, in contrast, exhibits a more dissipative behavior. Fig. 1(b) depicts the temporal evolution of the spatially averaged viscosity ratio μ_t/μ_l. Although the trend is similar for both models, the turbulent viscosity of the l^2-ω-DDES is significantly higher than that of the iDDES, even when comparing the fine grid of the l^2-ω-DDES with the coarse grid of the iDDES. This explains the observed dissipative behavior.

The DIHT test case is often used to calibrate the model constant C_{DES}. Reducing C_{DES} of the l^2-ω-DDES might lead to a better energy decay prediction. However, Reddy et al. [12] noted that reducing C_{DES} increases other problems such as LLM. Hence, the following simulations are performed with the original value of $C_{\mathrm{DES}} = 0.12$.

4.2. Fully developed turbulent channel flow

A fully developed turbulent channel flow between two flat plates at a bulk Reynolds number based on the channel half width of $Re_b = 125.000$ is considered. This corresponds to a friction Reynolds number of $Re_\tau \approx 5200$. Results are compared to the DNS data of Lee and Moser [51]. Periodic boundary conditions are applied in both the stream- and the spanwise direction. The channel has a half width of $\delta = 0.015\,\mathrm{m}$ and its dimensions are $16\delta \times 2\delta \times 6\delta$. The spacing of the grid used for the simulations is $(\Delta x/\delta, \Delta z/\delta) = (0.1, 0.05)$. Thus, the nominal resolution in wall units is $(\Delta x^+, \Delta z^+) = (520, 260)$. In the wall-normal direction it is ensured that $\Delta y^+ \leq 1$ directly at the wall. This grid would be too coarse and not sufficient for wall-resolved LES. However, the resolution is typical for DDES grids of turbulent channels, e.g. [39], and therefore sufficient for a comparison of the two hybrid methods. In order to remove the initial transients, the simulations are run for more than 80

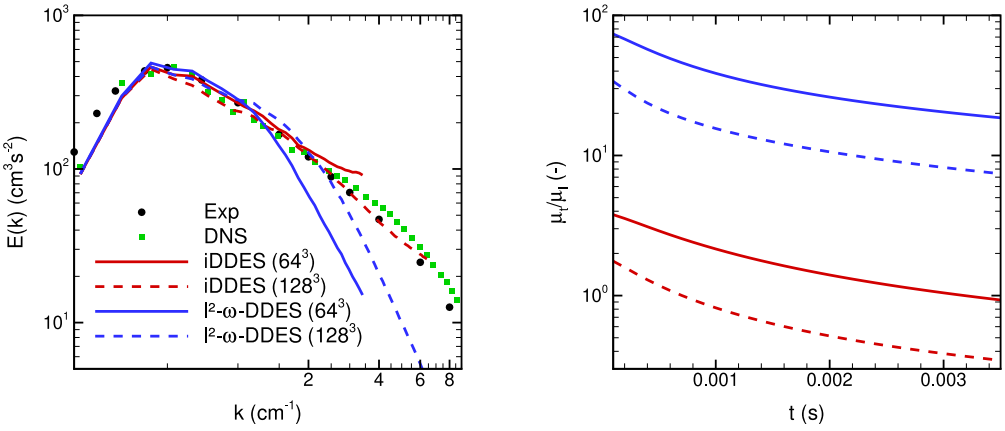

(a) Energy spectrum (b) Viscosity ratio

Fig. 1. Comparison of energy spectra and temporal evolution of spatially averaged viscosity ratio in DIHT predicted by iDDES and l^2-ω-DDES on different grids. *Source:* Experimental data from Comte-Bellot and Corrsin [48], DNS data from Wray [49].

non-dimensional time units $t^* = t\,u_\tau/\delta$. Afterwards, averaged flow fields are recorded for $t^* > 80$.

The flow is driven by a time-dependent forcing that ensures that the bulk Reynolds number is kept constant. Hence, the friction Reynolds number is part of the solution and can be used for validation. Both hybrid RANS/LES models slightly underpredict the target value of $Re_\tau = 5189$. The deviations are 2.2% for the iDDES and 4.0% for the l^2-ω-DDES. Thus, both simulations show an acceptable behavior.

Profiles of the stream-, span- and timewise averaged non-dimensional velocity $u^+ = \langle u\rangle/u_\tau$ are depicted in Fig. 2(a). The velocity is normalized with the friction velocity u_τ. In the viscous sublayer near the wall, both models coincide. However, the iDDES underpredicts the DNS data in the buffer and the log-layer, which is probably caused by the rather early switch from RANS to LES mode that affects the RANS log-layer. At the RANS-LES interface, both models exhibit a characteristic shift of the velocity profile known as LLM [9]. Therefore, the velocity at the center of the channel is slightly overpredicted. Both, iDDES and l^2-ω-DDES are designed to alleviate the issue of LLM [11,12]. However, LLM seems to be also dependent on the numerical solver [42], which might be the cause for its occurrence in this application.

Fig. 2(b) displays the ratio of turbulent to laminar viscosity along the wall-normal direction as well as the DES mode. The latter quantity indicates whether the model operates as RANS (DES mode = 0) or as LES (DES mode = 1). Anything in between is called gray area. For the investigated channel flow, the DES modes agree with the corresponding shielding functions of iDDES and l^2-ω-DDES. Both models use a k-ω model as background RANS model. Hence, near the wall, the viscosity ratios coincide. The turbulent viscosity reaches its maximum at the location where the transition from RANS to LES begins. Compared with the l^2-ω-DDES, this transition starts earlier for the iDDES and, accordingly, its maximal turbulent viscosity is significantly lower. On the other hand, the transition region ($0.01 <$ DES mode < 0.99) is significantly wider for the iDDES. Between $y/\delta \approx 0.3$ and the center of the channel, both models operate in LES mode. However, a significant difference is that the viscosity ratio of the l^2-ω-DDES at the center is approximately 6.5 times higher than of the iDDES. This follows from the different formulations and has already been observed for the local equilibrium values discussed in Section 3.3.

Fig. 2(c) displays the total normalized shear stresses as well as their corresponding modeled (subgrid-scale) and resolved parts. Time-averaging of the streamwise momentum equation yields the relationship $\langle u'v'\rangle/u_\tau^2 = y/\delta - 1$ for the total normalized shear stress [52]. Both models accurately predict the total shear stress. However, over the entire channel height, the absolute value of the resolved part of the l^2-ω-DDES is lower than that of the iDDES. In contrast, the contribution of the modeled part to the total shear stress is greater for the former. Hence, the resolved shear stress balances the modeled one. This behavior does not necessarily mean that iDDES outperforms l^2-ω-DDES. Instead, this is a consequence of the reduced turbulent viscosity of the iDDES and the correspondingly reduced subgrid-scale shear stresses.

The total turbulent kinetic energy is depicted in Fig. 2(d). Again, this quantity is composed of a resolved and a modeled part and is defined as $K = 0.5\langle u_i'u_i'\rangle + \langle k\rangle$. Time-averaging is denoted by $\langle\cdot\rangle$. The modeled turbulent kinetic energies are calculated according to Eqs. (7) and (26), respectively. Neither of the two models matches the location of the near-wall peak of the DNS, which is a disadvantage due to the underlying assumptions of the RANS method. However, the iDDES correctly predicts the maximum value. Over almost the entire channel height, the modeled part of the total turbulent kinetic energy is higher for the l^2-ω-DDES compared to the iDDES. This is consistent with the analysis of the subgrid formulation at local equilibrium conditions presented in Section 3.3. Thus, for the l^2-ω-DDES, the term $\langle k\rangle$ contributes significantly to K and leads to the correct prediction of K over the whole LES region. As its resolved part is not sufficient for a correct prediction of K, the iDDES underpredicts this quantity in that range.

Fig. 3 shows normalized instantaneous vorticity magnitudes in three planes parallel to the wall. In each case, the results of the iDDES are displayed on the left side and those of the l^2-ω-DDES on the right side. The top row presents the results at a non-dimensional wall distance of $y/\delta = 4.5 \times 10^{-3}$, which is in the near-wall region where both models operate in RANS mode. Both models exhibit rather elongated streaks, with iDDES being finer scaled. These streaks are particularly pronounced in the l^2-ω-DDES and can almost be described as so-called "super-streaks" [53]. At $y/\delta = 0.23$, which is located at the interface between RANS and LES mode, both models already exhibit fine-scale structures. However, the predicted vortical structures of the l^2-ω-DDES are still elongated and smoother compared with iDDES. This is probably caused by the later shift to LES. Near the center of the channel, shown at the bottom of Fig. 3, both models show quite similar vorticity distributions.

A more quantitative assessment of the above observations is obtained from streamwise two-point correlations of the streamwise velocity component at the same wall distances. These are depicted in Fig. 4. The two-point correlation, as defined by Pope [54], is calculated from

$$B_{uu}(x_0) = \langle u'(x)u'(x_0 + x)\rangle \tag{37}$$

and normalized by u_{rms}^2. In this case, it is independent from the location x_0. Two-point correlations are an indicator of the streamwise extent of

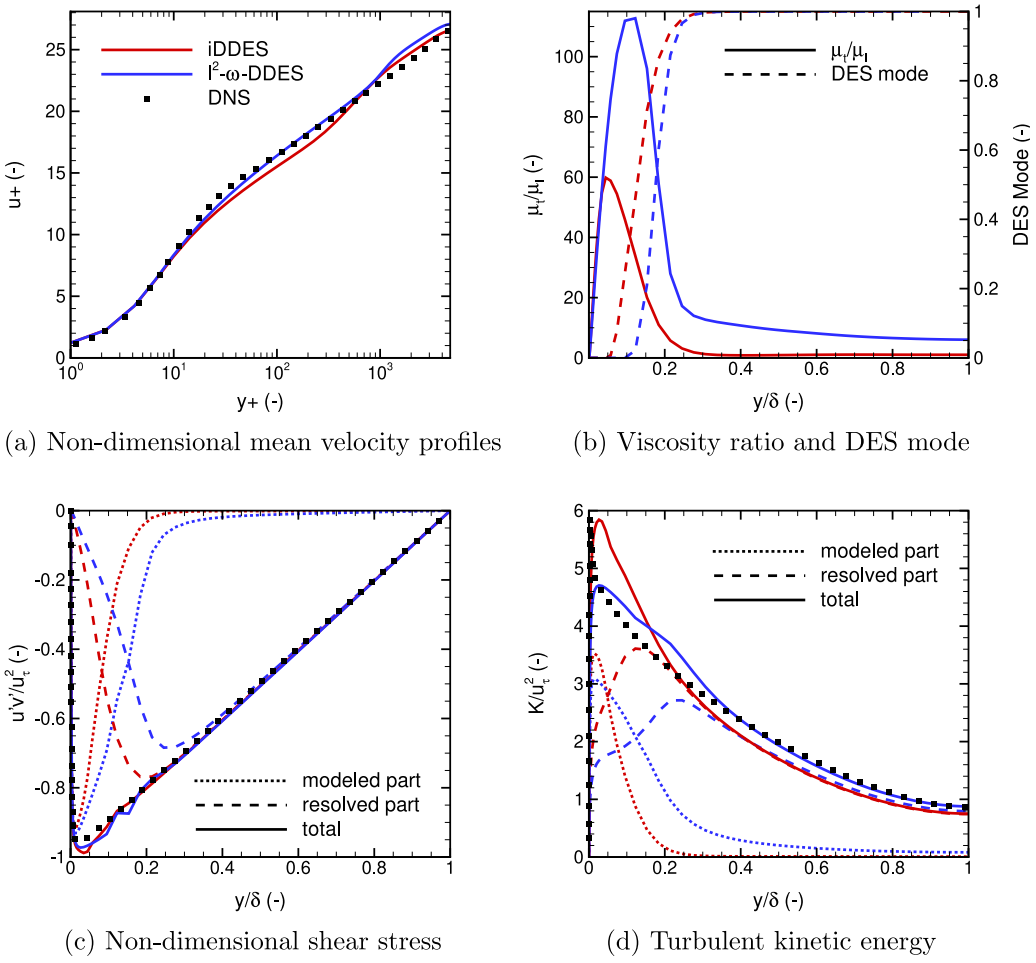

(a) Non-dimensional mean velocity profiles

(b) Viscosity ratio and DES mode

(c) Non-dimensional shear stress

(d) Turbulent kinetic energy

Fig. 2. Comparison of iDDES and l^2-ω-DDES for a fully developed turbulent channel flow.
Source: DNS data from Lee and Moser [51].

vortical structures. In contrast to the observations of Davidson [52], the two-point correlations vary across the channel height especially for the l^2-ω-DDES. Closer to the wall, the two-point correlations do not decrease as fast. The vortical structures become more elongated in streamwise direction near the wall. As already observed, "super-streaks" are formed close to the wall in the l^2-ω-DDES. With exception of the channel center, the l^2-ω-DDES two-point correlation values are considerably higher than that of the iDDES and the distances required to decrease to values of $B_{uu} = 0.2$ are nearly doubled. Close to the center of the channel both DDES techniques behave similarly. In general, the iDDES predicts vortices with a smaller spatial extent. However, these finer scaled structures do not necessarily result in a better prediction of averaged quantities. The differences in size of vortical structures and two-point correlations can be attributed to the increased turbulent viscosity of the production-limited l^2-ω-DDES as well as differences in the location of the transition region from RANS to LES.

Next we analyze, how close the simulated turbulent quantities are to values obtained under local equilibrium assumptions. Thus, the parameters $(k - k^{eq})/k^{eq}$ and $(\omega - \omega^{eq})/\omega^{eq}$ are depicted in Fig. 5. These also show where transport is dominant. As similar trends are observed for both techniques, this analysis is restricted to the iDDES. For k, transport effects dominate and there are only few locations mainly in the center of the channel where k is close to local equilibrium. Transport plays a much smaller role for ω, as this quantity is relatively close to local equilibrium over the entire channel. The different behavior of these two variables supports the annotations made by Kok et al. [46] and Yan et al. [47] that it is unlikely that both k and ω are at local equilibrium simultaneously. In both hybrid RANS/LES methods the k-equation is modified, whereas the ω-equation remains unaltered. Consequently, the production and dissipation terms of both equations are no longer modeled analogously causing the observed behavior. This is also noted in [46].

Fig. 6 shows the normalized difference between the simulated turbulent viscosities and the ones obtained under local equilibrium assumptions calculated from Eqs. (34) and (36), respectively. The equation for the iDDES was derived under the assumption that k and ω are at local equilibrium. In the whole LES area, turbulent viscosities of the l^2-ω-DDES are close to equilibrium. This is not surprising because μ_t only depends on ω, which shows a near-equilibrium behavior, too. Only a few exceptions exist. The results are in line with the objective of Reddy et al. [12], who designed this hybrid model to perform similar to a classical Smagorinsky-LES in such flow regions. Compared with the l^2-ω-DDES, the iDDES deviates much more from equilibrium. Especially near the RANS-LES interface turbulent viscosity values are significantly increased. As shown above, transport effects play an important role for k, while ω is much closer to local equilibrium. Because iDDES uses both k and ω for the calculation of μ_t, a strong deviation from equilibrium occurs. Hence, the different approaches to calculate the turbulent viscosity (see Eqs. (24) and (31), where k is used by the iDDES only) cause the stronger deviations from equilibrium in case of the iDDES and a stronger impact of transport.

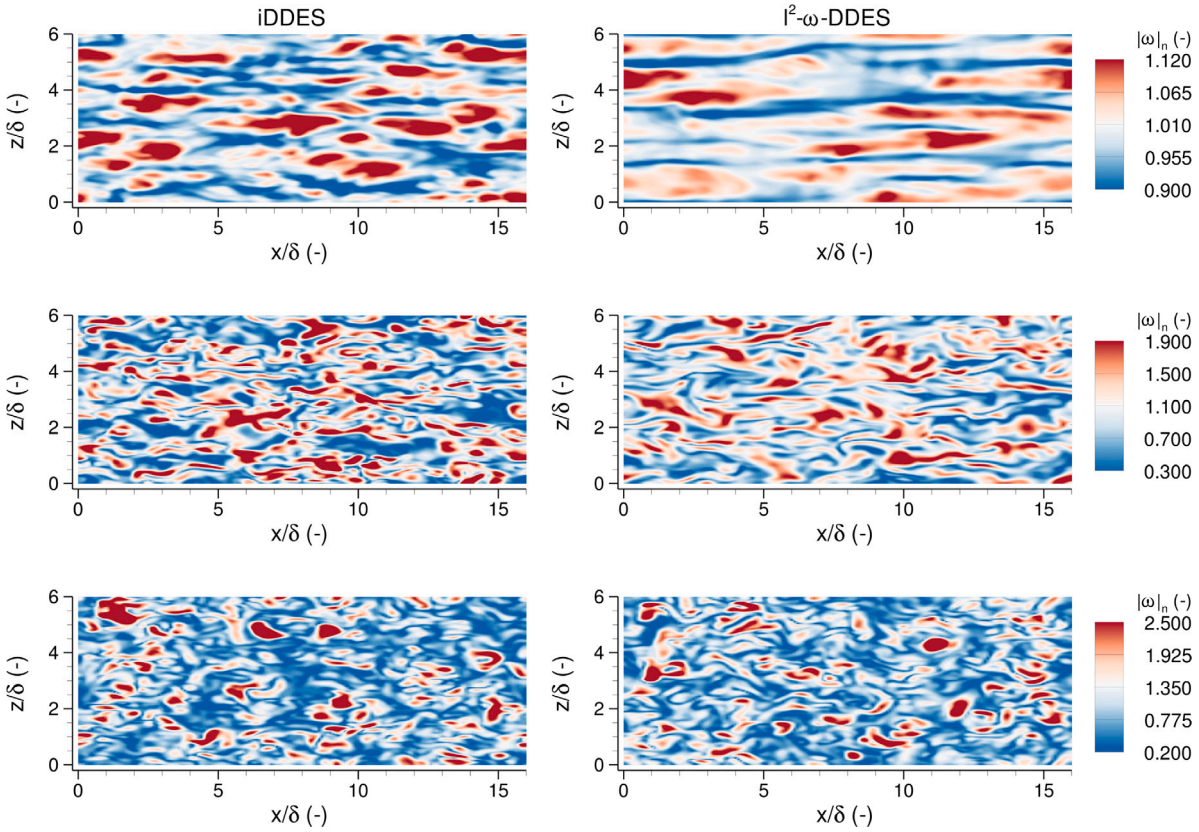

Fig. 3. Contours of normalized instantaneous vorticity magnitude along xz-planes in the turbulent channel. The vorticity magnitude is normalized with the spatially averaged vorticity magnitude in the given plane. Left: iDDES; Right: l^2-ω-DDES. From top to bottom: $y/\delta = 4.5 \times 10^{-3}$, $y/\delta = 0.23$, $y/\delta = 1.0$.

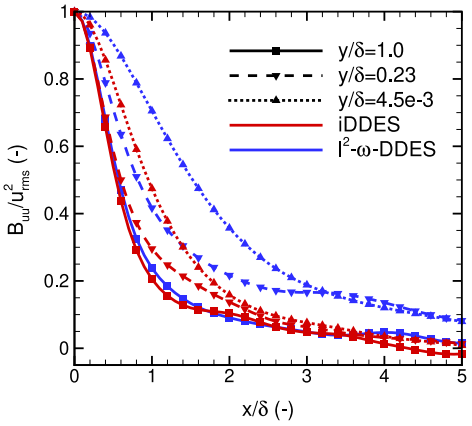

Fig. 4. Normalized two-point correlations of the streamwise velocity component in streamwise direction of iDDES and l^2-ω-DDES for different wall distances. The symbols mark every second grid point.

4.3. Backward-facing step

The last non-reactive test case is the BFS flow experimentally investigated by Driver and Seegmiller [55] and Driver et al. [56]. This is a rather important validation test case for hybrid RANS/LES models as a transition from RANS to LES must occur near the step. The step has a height of $H = 1.27\,\mathrm{cm}$ and it is located at $x/H = 0$. At that location, the flow separates and a recirculation zone develops at the lower wall. Air enters the domain with a mean freestream velocity of $u_{\mathrm{ref}} = 44.2\,\mathrm{m\,s^{-1}}$ and a boundary layer thickness of $\delta_{\mathrm{ref}} = 1.9\,\mathrm{cm}$. This results in a Reynolds number based on step height and freestream velocity of $Re_H \approx 37.000$. The height of the inflow duct is $8H$, thus yielding an expansion ratio of 1.125.

The numerical domain starts $4H$ upstream of the step and extends to $30H$ downstream of the sudden expansion. The spanwise extent is $4H$. Periodic boundary conditions are applied in this direction. Both the velocity and the turbulent quantities at the inflow are calculated by a preceding steady-state RANS simulation in such a way that the experimental boundary layer thickness is matched.

The mesh consists of 2.76 million volumes and especially near the lower wall it is finely resolved. Sixty uniformly spaced cells are used for the spanwise direction, while the step is resolved with 80 volumes. For both DDES variants, the mesh and all boundary conditions are identical. After a time period that is sufficient to remove the initial transients, time-averaging of flow field variables is performed for more than 15 convective time units. The latter is defined as the convection

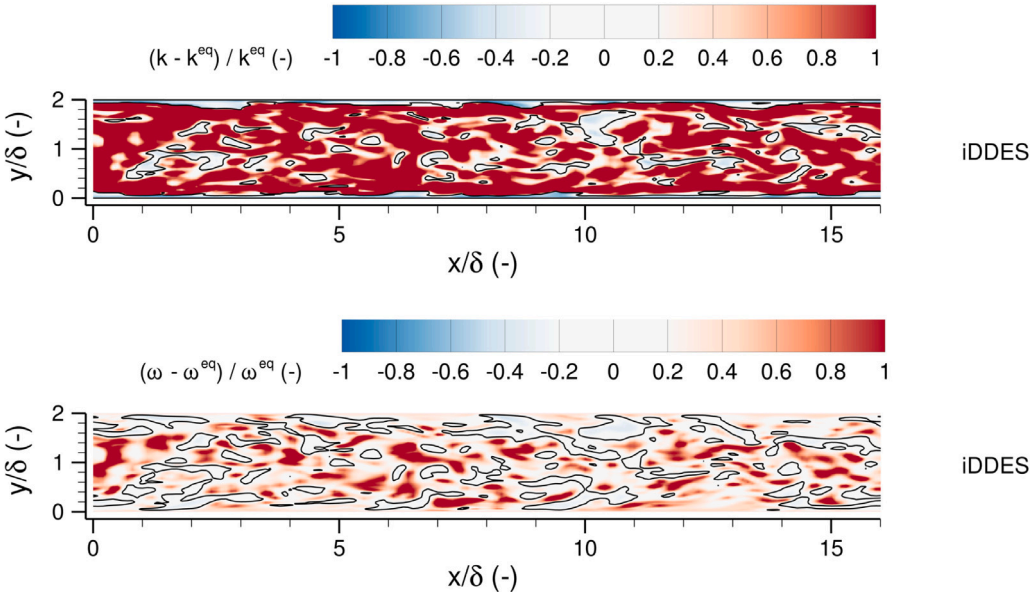

Fig. 5. Normalized difference between the simulated turbulent quantities and the values obtained by a local equilibrium assumption in a plane perpendicular to the wall for the turbulent channel flow using iDDES. Top: k; Bottom: ω. The black lines indicate the isolines where the turbulent quantity is at local equilibrium.

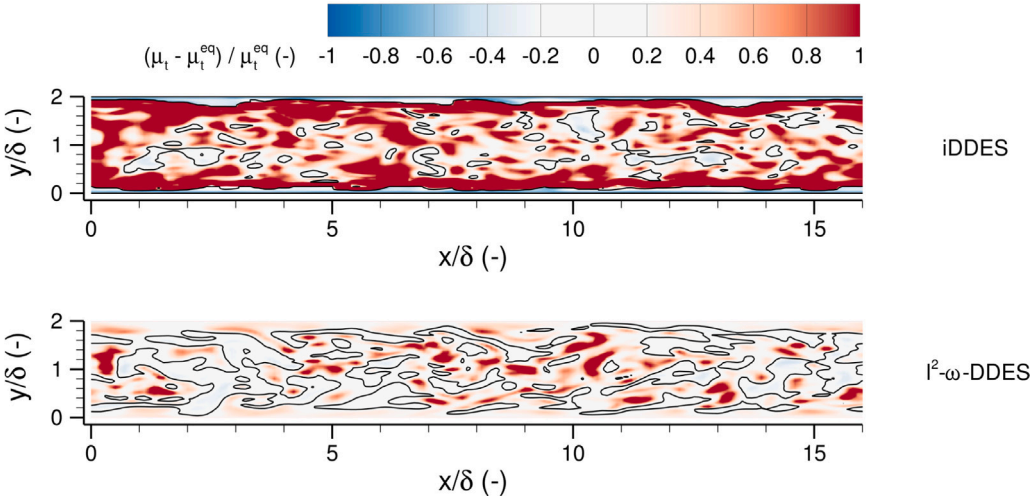

Fig. 6. Relative deviation of the simulated turbulent viscosity to the one obtained by an equilibrium assumption in a plane perpendicular to the wall for the turbulent channel flow using iDDES (top) and l^2-ω-DDES (bottom). The black lines indicate the isolines where the simulated turbulent viscosity is equal to the equilibrium turbulent viscosity.

time through the section downstream of the step at the mean convective speed.

The left-hand side of Fig. 7 depicts the skin friction coefficient c_f, defined as $c_f = 2\tau_w/(\rho u_{\text{ref}}^2)$, at the lower wall. Upstream of the step, the iDDES overestimates the measurements, whereas the l^2-ω-DDES correctly predicts the experimental friction coefficient. Both models use the same inflow condition. This behavior is caused by the usage of the additional empirical functions of the iDDES, in this particular case, the elevating function f_e defined in Eq. (17). Between the step and the reattachment point, both models show a similar behavior. Both hybrid RANS/LES methods slightly underestimate the minimal friction coefficient. The same applies to the length of the recirculation zone. While the experimental value is $6.26H$, the predictions of the recirculation lengths of the two hybrid models are $5.86H$ for the iDDES and $5.71H$ for the l^2-ω-DDES, respectively. Downstream of the reattachment point, iDDES and l^2-ω-DDES deviate. The latter exhibits a too steep increase and thus overestimates the measurements in the range between $x/H \approx 7.0$ and $x/H \approx 16$. In the rear part, both models match the experimental data very well.

The right-hand side of Fig. 7 shows the static pressure coefficient $c_p = (p - p_{\text{ref}})/(0.5\rho u_{\text{ref}}^2)$ at the lower wall. Both DDES variants differ only slightly from each other and, in addition, agree fairly well with the experimental data. The most notable difference is a slight overestimation of the measurements downstream of the reattachment point.

Profiles of the mean streamwise velocity at different locations are shown in the left-hand side of Fig. 8. Good agreement is obtained in comparison with the experiment. This also applies to positions with $x/H > 10$ (not shown here). The only deviations occur in the vicinity of the step where the velocity gradient is overpredicted. This seems to be a typical artifact of hybrid RANS/LES models as the delayed transition from RANS to LES mode hinders mixing.

The right-hand side of Fig. 8 displays the total axial Reynolds stresses at different positions. Upstream of the step, both models achieve a good agreement with the experimental data. However, the sudden increase of normal stresses shortly downstream of the step is not matched by any of the models and it takes until $x/H \approx 2$ for the maximum values to coincide. Again, the delayed transition from RANS to LES proves to be problematic. The maximum value

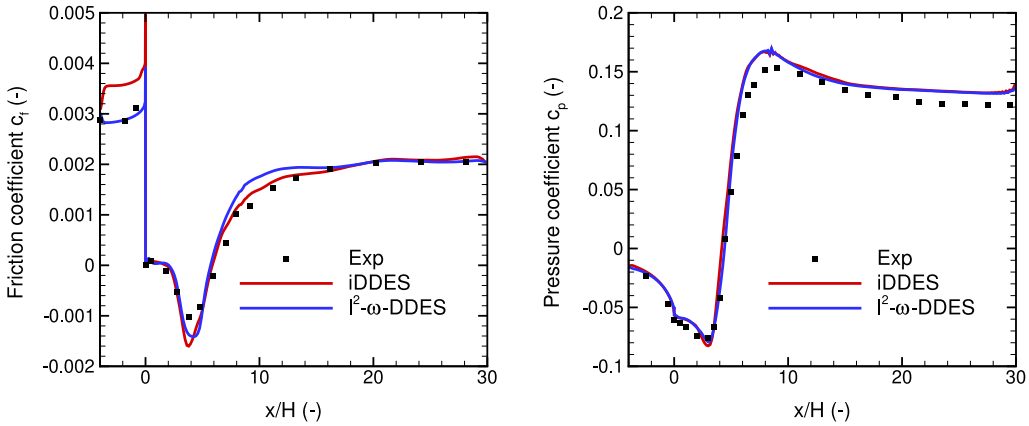

Fig. 7. Skin friction coefficient c_f (left) and wall static pressure coefficient c_p (right) at the lower wall.
Source: Experimental data from Driver and Seegmiller [55].

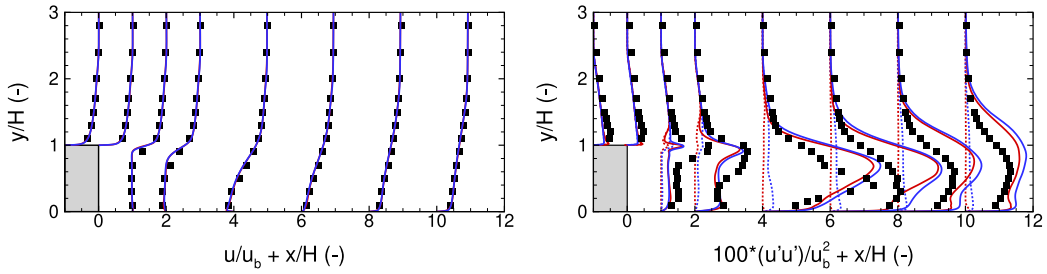

Fig. 8. Mean streamwise velocity normalized by u_{ref} (left) and normalized total axial Reynolds stresses (right). Same legend as Fig. 7. The modeled part of the normal stresses is displayed using a dotted line. Profiles are plotted at $x/H = -1.0$, 0.0, 1.0, 2.0, 4.0, 6.0, 8.0, 10.0.
Source: Experimental data from Driver and Seegmiller [55].

of the experimental turbulent Reynolds stresses starts to decrease at around $x/H \approx 4$. In both hybrid models, this behavior is delayed and takes place downstream of $x/H \approx 5$ and, hence, the normal stresses are strongly overestimated in the rear part. Besides, the location of the maximum value is shifted away from the wall compared to the experiment. In general, this behavior seems to be typical for DDES-type simulations as similar trends could also be observed for iDDES on much finer grids [57], too. For $x/H > 5$, the total axial normal stresses of the l^2-ω-DDES are slightly higher compared with iDDES. The reasons are the same as for the turbulent channel flow. The modeled part of any turbulent quantity is larger for the l^2-ω-DDES than for the iDDES, thus contributing significantly to the total quantity (see Fig. 8).

The ratio of turbulent to laminar viscosity is depicted in Fig. 9. In addition, this figure includes the isolines where the corresponding model is 90% in LES mode. As required, iDDES and l^2-ω-DDES operate in RANS mode at the upper wall as well as at the lower wall upstream of the step. The heights of the RANS modes are nearly the same for both models. Somewhat downstream of the step, both models switch from RANS to LES. This delay of transition, which is typical for such kind of simulations [58], is longer in case of the iDDES with higher eddy viscosity values in the wake of the boundary layer downstream of the step. However, at the lower wall, the WMLES capabilities of the iDDES take effect, leading to an extremely small RANS range. In contrast, the l^2-ω-DDES shows a significantly broader RANS region. These differences are extremely important if not only a backward-facing step is simulated, but a larger geometry where the flow should return to RANS mode after reattachment at the lower wall in order to allow higher cell aspect ratios again further downstream. In addition, the RANS mode of the l^2-ω-DDES is shaped irregularly and is strongly time-dependent due to the turbulent nature of the flow downstream of the step. The eddy viscosity values in this region are still lower than upstream of the step, thereby enabling the formation of vortices. Compared with the iDDES, l^2-ω-DDES exhibits higher levels of eddy viscosity downstream of the step. This also has a significant effect on the instantaneous flow field. Similar to the channel flow, the vortex structures of the iDDES are significantly smaller than the ones of the l^2-ω-DDES (not shown).

Fig. 10 shows the relative deviation of the turbulent viscosities to the ones if local equilibrium is assumed. The figure on the left side depicts the iDDES, while the l^2-ω-DDES is shown on the right. In both cases, the turbulent viscosities deviate significantly from their equilibrium counterparts, especially in the central part of the channel, even though LES mode is active there (see Fig. 9). This behavior is caused by the inflow conditions as all inflow values are calculated using a preceding steady-state RANS simulation. In the central part of the channel, almost no resolved turbulent content develops. Thus the magnitude of the traceless mean strain tensor is quite small and consequently transport effects dominate. Downstream of the step, the l^2-ω-DDES becomes more of a Smagorinsky model, while only few small regions are close to equilibrium for the iDDES. This behavior is identical to that observed for the turbulent channel flow and demonstrates the differences between the two DDES techniques in case of strongly separated flows.

5. PennState preburner combustor

5.1. Test case description

The PennState preburner combustor is a laboratory-scale rocket combustion chamber experimentally investigated at the Pennsylvania State University [59,60] with the goal to provide data for the verification and validation of numerical codes. Hence, this is a frequently simulated test case [1,2,61–66]. Various modeling approaches with varying complexity ranging from pure RANS/URANS to LES have been

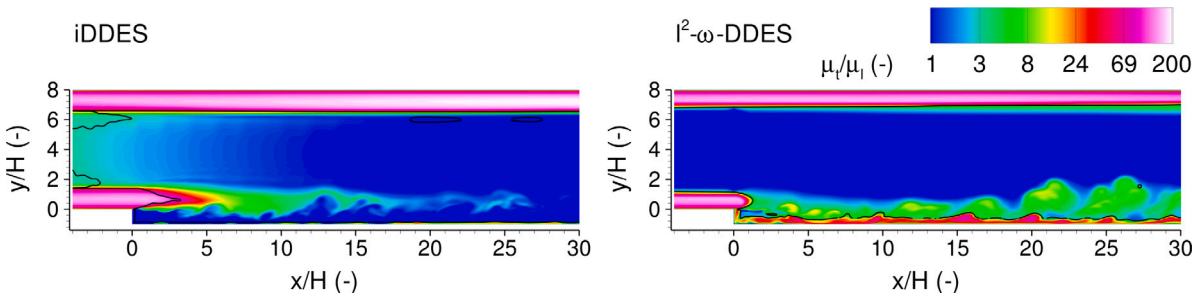

Fig. 9. Contour plot of instantaneous viscosity ratio. The black lines indicate the isolines where the corresponding model is 90% in LES mode. Left: iDDES; Right: l^2-ω-DDES. Note that a non-linear scale for the contour levels is used.

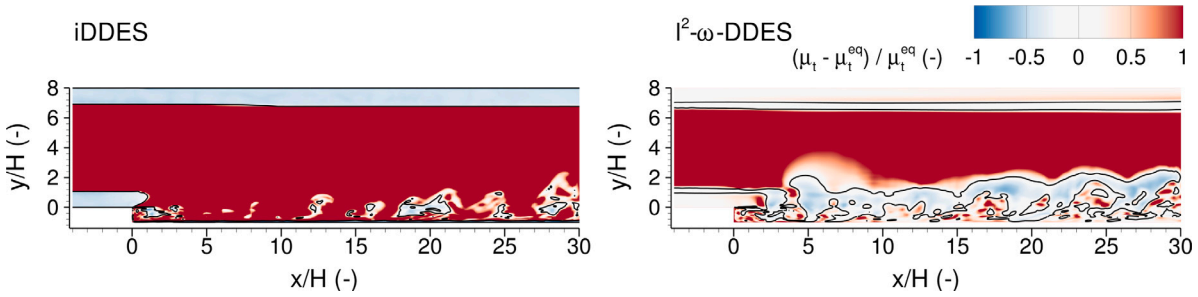

Fig. 10. Comparison of the difference between the simulated turbulent viscosities with the ones if local equilibrium of the turbulence equations is assumed. Left: iDDES; Right: l^2-ω-DDES. The black isolines indicate where the simulated turbulent viscosity is equal to the equilibrium turbulent viscosity.

Table 1
Inflow parameters of the PennState preburner combustor.

	Oxidizer stream	Fuel stream
Inner diameter (mm)	–	6.30
Outer diameter (mm)	5.26	7.49
Gas composition (–)	0.945 (O_2)	0.402 (H_2)
	0.055 (H_2O)	0.598 (H_2O)
Total mass flow rate (kg/s)	0.0904	0.0331
Temperature (K)	700	811
Bulk velocity (m/s)	154	764
Reynolds number (–)	604,000	169,000

used. The cylindrical combustion chamber has a length of 285.75 mm and a diameter of 38.1 mm. The diameter of the nozzle is 8.2 mm. Gaseous hydrogen and gaseous oxygen are preburned in a fuel- and a oxidizer-rich preburner, respectively, and are supplied to the main combustion chamber through a single coaxial injector. The global oxidizer-to-fuel ratio (O/F) is ∼6.7. The oxidizer post is recessed 0.43 mm behind the faceplate. Geometrical dimensions, gas compositions and flow characteristics of the coaxial injector are summarized in Table 1. For a more detailed description of the test case, the reader is referred to [59,60].

The used computational grid consists of approximately 19.6 million volumes, divided into 39 blocks. The injector including the recess area accounts for 5.4% of the volumes, while 4.6% are used to discretize the nozzle. The remaining 17.7 million volumes are used for the combustion chamber. In radial direction, the oxidizer post tip is resolved by 16 volumes. Apart from exceptions at the faceplate and shortly downstream of it, the wall grid spacing in radial direction of the chamber satisfies $\Delta y^+ < 1$. The experimental data set provides wall temperatures and wall heat fluxes. While the latter serves as validation data, the former is used to prescribe the temperature profile along the combustion chamber wall. The injector walls are assumed to be adiabatic, while the oxidizer post tip and the faceplate are treated isothermal with a temperature of 755 K. At the inlet, mass flow rates, as stated in Table 1, are specified. A supersonic outflow condition is imposed at the outlet.

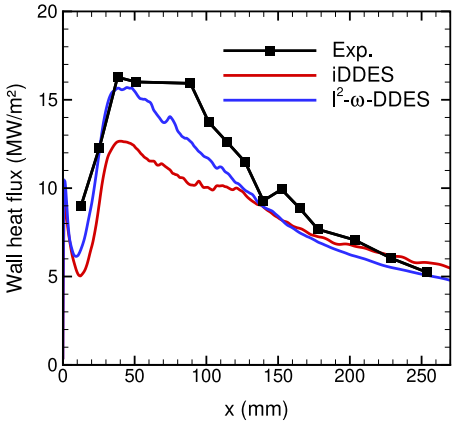

Fig. 11. Measured and simulated wall heat fluxes along the chamber wall.
Source: Experimental data from Pal et al. [60].

Applying the l^2-ω-DDES in its original formulation to the injector tube flows caused a strongly delayed development of Kelvin–Helmholtz instabilities and subsequently an unphysical flame structure. To overcome this issue, the l^2-ω-DDES is forced to operate almost entirely in LES mode (DES mode > 95%) in the coaxial injector. This is done by modifying the lengthscale l_{DDES}. Accordingly, the shielding function is no longer responsible for switching between RANS and LES, but instead, away from the walls, almost full LES mode is enforced. However, this procedure only applies to the injector and not the combustion chamber itself. This approach prevents the excessive production of k and thus downstream of the injector vortices can be formed more quickly. A similar procedure has already been used for this test case by Huo and Yang [64]. Due to its much lower μ_t values, this modification was not required for the iDDES.

Both simulations are performed with a constant physical time step size of $\Delta t = 1 \times 10^{-8}$ s and are averaged over 1.66 million iterations. This corresponds to 16.6 ms or two flow through times. Based on the

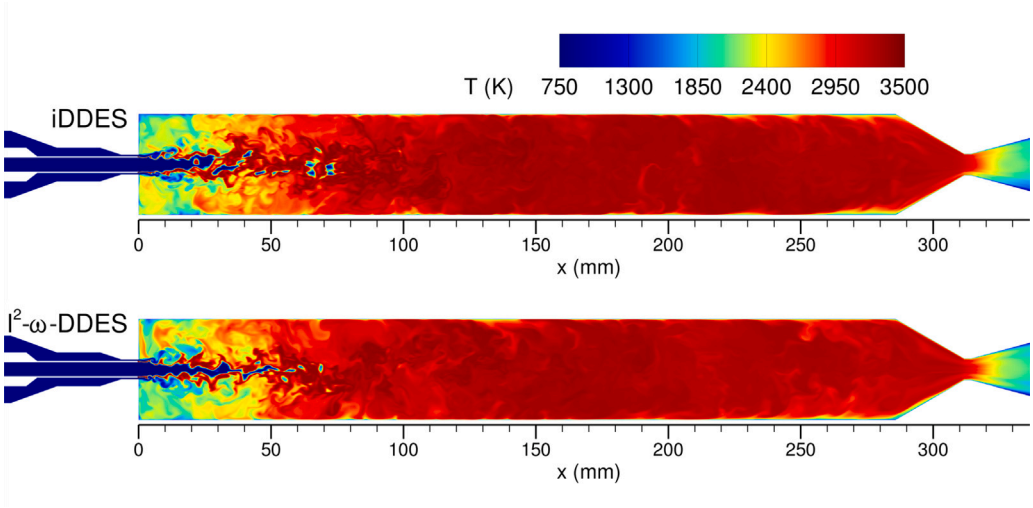

Fig. 12. Calculated instantaneous temperature distributions in the PennState preburner combustor for the iDDES (top) and l^2-ω-DDES (bottom) in the cross section $z = 0\,\text{mm}$.

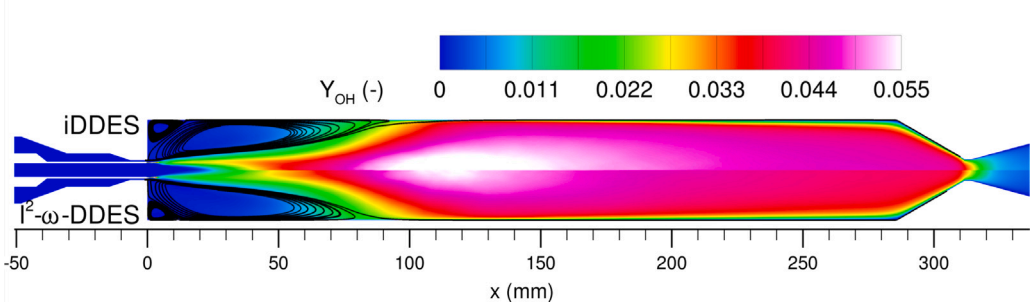

Fig. 13. Comparison of time- and circumferentially averaged hydroxyl mass fractions. Top half: iDDES; Lower half: l^2-ω-DDES. Streamlines are imposed to highlight the recirculation zones.

bulk mass flow, Tucker et al. [62] defined the flow through time to be 8.3 ms.

In contrast to the previous test cases, the DDES models now have to deal with high pressure and strong density gradients as well as compressible and supersonic flow.

5.2. Results

Fig. 11 depicts the time- and circumferentially averaged wall heat fluxes along the chamber wall of both simulations. In addition, the experimental data from Pal et al. [60] is given. It is worth noting that the simulation results contain no modeled part as it is negligible at the wall. The iDDES reaches a maximum wall heat flux of 12.7 MW m^{-2}. Thus, the experimental maximum is underestimated by 22.3%. Accordingly, the wall heat flux prediction of the iDDES up to $x \approx 140\,\text{mm}$ is too low. However, in the rear part of the combustion chamber, the iDDES shows a good agreement with the experimental data. In contrast, the l^2-ω-DDES correctly predicts the rise of the wall heat flux in the front part. In addition, the peak value and its location nearly match the experimental data. The maximum wall heat flux is underestimated by 3.6% only. The experiment shows a nearly constant high heat flux between $x \approx 40\,\text{mm}$ and $x \approx 90\,\text{mm}$. In the simulation, such a large plateau is not visible. Instead, a smaller one with a length of approximately 15 mm exists. Again, there is a good agreement between the l^2-ω-DDES and the experiment in the rear part of the chamber. With respect to the wall heat flux, the l^2-ω-DDES performs significantly better than the iDDES.

The wall heat flux depends on both the wall temperature gradient and the thermal conductivity at the wall. Instantaneous temperature distributions are shown in Fig. 12. Both models exhibit a similar behavior. Behind the injector lip, for slightly more than half the diameter of the oxidizer tube, no coherent vortical structures are visible. Masquelet and Menon [67] attribute this behavior to the stability of the high speed hydrogen stream. However, as such a behavior is not observed in the pure LES of Oefelein [61], this might be an artifact of the gray-area problem in the hybrid RANS/LES models. This refers to the problem that the development of turbulent structures is delayed at the switch from RANS to LES. Although the l^2-ω-DDES was formally forced to operate in LES mode, this issue still persists as the values of k are still comparatively high. Further downstream, typical Kelvin–Helmholtz instabilities occur, causing small-scale vortical structures. The cold oxygen core breaks down at around $x \approx 50\,\text{mm}$. Still, cold oxygen bubbles exist in the first third of the combustion chamber. This is similar to the simulations of Ma et al. [65]. Due to the comparably large distance of the injector from the outer walls, which is not the case in real rocket combustors, a large outer recirculation zone exists in the first part of the combustor. It extends up to approximately one third of the chamber and has a length of 100.9 mm for the iDDES and 87.6 mm for the l^2-ω-DDES. Both recirculation zones are highlighted in Fig. 13. There is a relatively large difference between both DDES techniques. As the end of the experimental high wall heat flux plateau is located at $x = 88.9\,\text{mm}$, it demonstrates the importance of the recirculation zone on the wall heat flux prediction. The recirculated gas consists of hydrogen and hot combustion products. Compared with the l^2-ω-DDES, the iDDES predicts higher temperatures in the recirculation zone. However, this does not hold for the near-wall region, where the temperatures of the l^2-ω-DDES are higher due to enhanced mixing and heat conduction. Accordingly, the wall temperature gradient of the l^2-ω-DDES is higher as well. In the rear part, a nearly homogeneous temperature distribution exists, with higher values for the iDDES. This

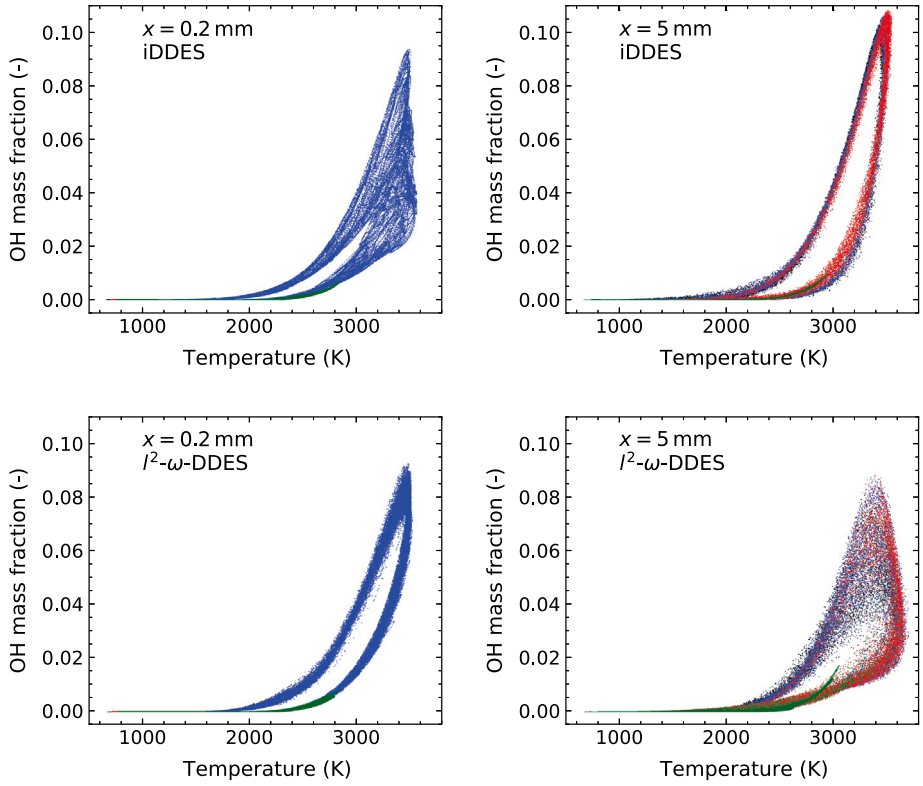

Fig. 14. Scatter plots of instantaneous hydroxyl mass fraction versus temperature along vertical planes at $x = 0.2\,\text{mm}$ (left) and $x = 5.0\,\text{mm}$ (right) for the PennState preburner test case. Top: l^2-ω-DDES; Bottom: iDDES. The points are extracted from multiple instantaneous snapshots and are colored by the respective radius (black: $r \leq 2.63\,\text{mm}$, blue: $2.63\,\text{mm} < r \leq 3.15\,\text{mm}$, red: $3.15\,\text{mm} < r \leq 3.745\,\text{mm}$, green: $r > 3.745\,\text{mm}$).

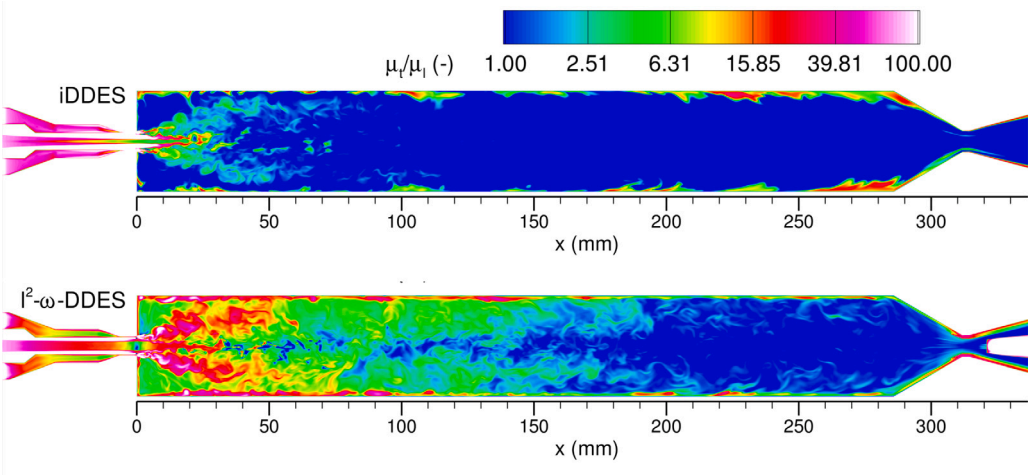

Fig. 15. Ratio of instantaneous turbulent to molecular viscosity in the center-plane of the PennState preburner combustor using iDDES (top) and l^2-ω-DDES (bottom). Note that a non-linear scale for the contour levels is used.

also explains the slightly higher wall heat flux of the iDDES downstream of $x \approx 160\,\text{mm}$ in comparison with the l^2-ω-DDES.

Time- and circumferentially averaged mass fraction distributions of the hydroxyl radical are shown in Fig. 13. For hydrogen and oxygen, only minor differences occur. The same holds for the mass fraction of water. Hence, these major species are not shown. For both DDES techniques, the cold oxidizer-rich core shows a similar behavior. Using an arbitrary cutoff of 10% oxygen mass fraction, the oxidizer-rich core has a length of 84.8 mm in the l^2-ω-DDES and a length of 88.2 mm in the iDDES. As depicted in Fig. 13, the iDDES shows higher levels of hydroxyl mass fraction throughout the whole chamber. This indicates that, although the flames look alike, the combustion processes of the two models differ.

In order to further highlight these differences in the combustion process, the thermochemical state space is investigated. Fig. 14 shows scatter plots of the instantaneous hydroxyl mass fraction versus temperature for both models. Plotted are instantaneous values from all volumes located in two vertical planes shortly downstream of the injector lip. Especially for $x = 0.2\,\text{mm}$ in the iDDES and for $x = 5\,\text{mm}$ in the l^2-ω-DDES, a strong scattering occurs. These plots show that, despite

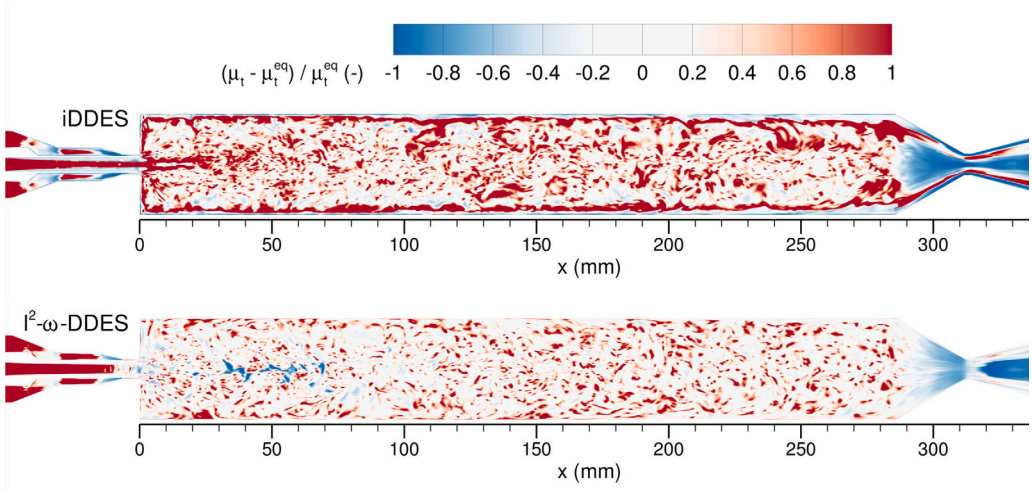

Fig. 16. Relative deviation of the simulated turbulent viscosity to the one obtained by an equilibrium assumption in the center-plane of the PennState preburner combustor. Top: iDDES; Bottom: l^2-ω-DDES.

the high pressure of nearly 50 bar and the corresponding fast chemistry, at these positions in the combustion chamber strong chemical non-equilibrium exists. However, the positions of these phenomena differ. The iDDES shows such a non-equilibrium behavior directly downstream of the injector lip, where the l^2-ω-DDES is close to chemical equilibrium. In the latter model chemical non-equilibrium develops further downstream. As will be shown below, turbulent viscosities of the l^2-ω-DDES are generally significantly higher than the ones of the iDDES, especially in the first half of the combustion chamber. Apart from its influence on the flow field, turbulent viscosity also affects combustion modeling. In this work, an APDF model is utilized to account for TCI. Besides LES filter width, the turbulent viscosity is also included in the source term for both σ_T and σ_Y in the LES region [68]. Hence, the resulting values of σ_T and σ_Y differ and cause a different combustion behavior.

Ratios of laminar to turbulent viscosity of both approaches are compared in Fig. 15. Similar to the non-reactive test cases presented above, the l^2-ω-DDES exhibits higher levels of turbulent viscosity within the whole combustion chamber. In both cases, the highest values are reached shortly downstream of the injector lip. In case of the iDDES, these high values decay quickly, whereas the decline for the l^2-ω-DDES is much slower. This can be attributed to the different modifications of the corresponding transport equations of the turbulence variables. The iDDES places a lower limit on the dissipation term of the k-equation, thus increasing the dissipation of k in the LES mode. This, in turn, leads to a faster decrease in turbulent viscosity. For l^2-ω-DDES, high values of turbulent viscosity extend up to the chamber walls, thus affecting the recirculation zone. In addition, these differences cause the different combustion behaviors, as described before. It is worth noting that the l^2-ω-DDES switches back to RANS mode in the divergent part of the nozzle. This might be due to grid coarsening in that region. Hence, the viscosity ratio reaches values clearly above 100. This is in contrast to the iDDES, which despite a relatively coarse mesh remains in LES mode.

A comparison of the differences between simulated turbulent viscosities with corresponding local equilibrium values obtained from Eqs. (34) and (36) is displayed in Fig. 16. In both cases, irregular and small-scale patterns occur. Nonetheless, some characteristic features are apparent. Results from the previous, non-reactive test cases showed that the LES mode of the l^2-ω-DDES operates more closely to equilibrium compared with iDDES. This is also true for the PennState preburner combustor. Similar to the observations for the channel flow, the relative deviation of the turbulent viscosity to the one obtained at local equilibrium is significantly increased close to the RANS-LES interface. This even holds in the convergent-divergent nozzle. In the convergent part of the nozzle, both models exhibit turbulent viscosities that are lower than expected at equilibrium. As the flow accelerates, the magnitude of the traceless mean strain rate tensor increases and accordingly the equilibrium turbulent viscosity grows. Nevertheless, transport effects predominate. Overall, l^2-ω-DDES is again closer to equilibrium than iDDES.

6. Summary and conclusions

In this work, the dissipation-limited iDDES and the production-limited l^2-ω-DDES are compared. Four test cases, including one rocket combustion chamber, were simulated and analyzed.

For the non-reactive test cases mean quantities of both models show similar results. In addition, these results agree quite well with experimental or DNS data. Differences, both among themselves and in comparison with experiments or DNS, occur for second-order moments. However, results from both DDES techniques are quite good. Clear differences between iDDES and l^2-ω-DDES arise when comparing instantaneous snapshots of the flow. The vortical structures of the l^2-ω-DDES are coarser, caused by an increased turbulent viscosity of this approach compared to iDDES. That means that in pure LES regions, absolute values of the modeled part of any quantity are higher for the l^2-ω-DDES. These differences arise from the varying formulations, as shown in the theoretical part of the paper.

Another important difference is the degree of transported subgrid turbulence in LES mode. While the l^2-ω-DDES is relatively close to an algebraic Smagorinsky model, the transport of k causes significant deviations from local equilibrium values in case of the iDDES. This is observed in all test cases including the one with combustion. The differences between both DDES techniques are enhanced for the PennState combustion chamber. Due to the strong non-linearity of chemical kinetics, already small differences in mixing may induce changes in the temperature field and, as in the present case, in composition and size of burned gas recirculation. In case of the PennState combustion chamber, the l^2-ω-DDES clearly outperforms the iDDES as the wall heat flux agrees better with the experimental data.

CRediT authorship contribution statement

Timo Seitz: Software, Investigation, Visualization, Writing – original draft. **Peter Gerlinger:** Conceptualization, Project administration, Supervision, Writing – review & editing.

Declaration of competing interest

The authors declare that they have no known competing financial interests or personal relationships that could have appeared to influence the work reported in this paper.

Data availability

Data will be made available on request.

Acknowledgments

The authors gratefully acknowledge the Gauss Centre for Supercomputing e.V. (www.gauss-centre.eu) for funding this project by providing computing time on the GCS Supercomputer HAWK at High Performance Computing Center Stuttgart (HLRS) (www.hlrs.de).

References

[1] Lian C, Merkle CL. Contrast between steady and time-averaged unsteady combustion simulations. Comput & Fluids 2011;44(1):328–38. http://dx.doi.org/10.1016/j.compfluid.2011.01.032.

[2] Lempke M, Keller R, Gerlinger P. Influence of spatial discretization and unsteadiness on the simulation of rocket combustors. Internat J Numer Methods Fluids 2015;79(9):437–55. http://dx.doi.org/10.1002/fld.4059.

[3] Fröhlich J, von Terzi D. Hybrid LES/RANS methods for the simulation of turbulent flows. Prog Aerosp Sci 2008;44(5):349–77. http://dx.doi.org/10.1016/j.paerosci.2008.05.001.

[4] Chaouat B. The state of the art of hybrid RANS/LES modeling for the simulation of turbulent flows. Flow Turbul Combust 2017;99:279–327. http://dx.doi.org/10.1007/s10494-017-9828-8.

[5] Durbin PA. Some recent developments in turbulence closure modeling. Annu Rev Fluid Mech 2018;50(1):77–103. http://dx.doi.org/10.1146/annurev-fluid-122316-045020.

[6] Spalart PR, Jou WH, Strelets M, Allmaras SR. Comments on the feasibility of LES for wings, and on a hybrid RANS/LES approach. In: Liu C, Liu Z, editors. Advances in DNS/LES, Proceedings of the First AFOSR International Conference on DNS/LES. 1997, p. 137–47.

[7] Strelets M. Detached eddy simulation of massively separated flows. In: 39th Aerospace Sciences Meeting and Exhibit. AIAA Paper 2001-0879, American Institute of Aeronautics and Astronautics; 2001, http://dx.doi.org/10.2514/6.2001-879.

[8] Menter FR, Kuntz M. Adaptation of eddy-viscosity turbulence models to unsteady separated flow behind vehicles. In: McCallen R, Browand F, Ross J, editors. The aerodynamics of heavy vehicles: trucks, buses, and trains. Springer Berlin Heidelberg; 2004, p. 339–52. http://dx.doi.org/10.1007/978-3-540-44419-0_30.

[9] Nikitin NV, Nicoud F, Wasistho B, Squires KD, Spalart PR. An approach to wall modeling in large-eddy simulations. Phys Fluids 2000;12(7):1629–32. http://dx.doi.org/10.1063/1.870414.

[10] Spalart PR, Deck S, Shur ML, Squires KD, Strelets MK, Travin A. A new version of detached-eddy simulation, resistant to ambiguous grid densities. Theor. Comput. Fluid Dyn. 2006;20(3):181–95. http://dx.doi.org/10.1007/s00162-006-0015-0.

[11] Shur ML, Spalart PR, Strelets MK, Travin AK. A hybrid RANS-LES approach with delayed-DES and wall-modelled LES capabilities. Int J Heat Fluid Flow 2008;29(6):1638–49. http://dx.doi.org/10.1016/j.ijheatfluidflow.2008.07.001.

[12] Reddy KR, Ryon JA, Durbin PA. A DDES model with a Smagorinsky-type eddy viscosity formulation and log-layer mismatch correction. Int J Heat Fluid Flow 2014;50:103–13. http://dx.doi.org/10.1016/j.ijheatfluidflow.2014.06.002.

[13] Yin Z, Reddy KR, Durbin PA. On the dynamic computation of the model constant in delayed detached eddy simulation. Phys Fluids 2015;27(2):025105. http://dx.doi.org/10.1063/1.4907746.

[14] Yin Z, Durbin PA. An adaptive DES model that allows wall-resolved eddy simulation. Int J Heat Fluid Flow 2016;62:499–509. http://dx.doi.org/10.1016/j.ijheatfluidflow.2016.08.009.

[15] Bader SH, Yin Z, Durbin PA. A hybrid model for turbulence and transition, with a locally varying coefficient. Flow Turbul Combust 2022;108(4):935–54. http://dx.doi.org/10.1007/s10494-021-00308-4.

[16] Gerlinger P, Brüggemann D. Multigrid convergence acceleration for turbulent supersonic flows. Internat J Numer Methods Fluids 1997;24(10):1019–35. http://dx.doi.org/10.1002/(SICI)1097-0363(19970530)24:10<1019::AID-FLD528>3.0.CO;2-O.

[17] Gerlinger P, Möbus H, Brüggemann D. An implicit multigrid method for turbulent combustion. J Comput Phys 2001;167(2):247–76. http://dx.doi.org/10.1006/jcph.2000.6671.

[18] Gerlinger P, Stoll P, Kindler M, Schneider F, Aigner M. Numerical investigation of mixing and combustion enhancement in supersonic combustors by strut induced streamwise vorticity. Aerosp Sci Technol 2008;12(2):159–68. http://dx.doi.org/10.1016/j.ast.2007.04.003.

[19] Gerlinger P. Multi-dimensional limiting for high-order schemes including turbulence and combustion. J Comput Phys 2012;231(5):2199–228. http://dx.doi.org/10.1016/j.jcp.2011.10.024.

[20] Simsont YH, Gerlinger P. High order numerical simulation of the thermal load on a lobed strut injector for scramjet applications. Internat J Numer Methods Fluids 2016;82(7):417–36. http://dx.doi.org/10.1002/fld.4224.

[21] Seidl M, Aigner M, Keller R, Gerlinger P. CFD simulations of turbulent non-reacting and reacting flows for rocket engine applications. J Supercrit Fluids 2017;121:63–77. http://dx.doi.org/10.1016/j.supflu.2016.10.017.

[22] Lechtenberg A, Gerlinger P. REST HF-10 test case: Flame response to externally excitation of a methane driven rocket combustion chamber. In: 9th European Conference for Aeronautics and Aerospace Sciences. EUCASS, 2022, http://dx.doi.org/10.13009/EUCASS2022-6075.

[23] Jameson A, Yoon S. Lower-upper implicit schemes with multiple grids for the Euler equations. AIAA J 1987;25(7):929–35. http://dx.doi.org/10.2514/3.9724.

[24] Shuen J-S, Yoon S. Numerical study of chemically reacting flows using a lower-upper symmetric successive overrelaxation scheme. AIAA J 1989;27(12):1752–60. http://dx.doi.org/10.2514/3.10331.

[25] Shuen J-S. Upwind differencing and LU factorization for chemical non-equilibrium Navier-Stokes equations. J Comput Phys 1992;99(2):233–50. http://dx.doi.org/10.1016/0021-9991(92)90205-D.

[26] Gear CW. Numerical initial value problems in ordinary differential equations. Prentice Hall; 1971.

[27] Burden RL, Faires JD. Numerical analysis. Cengage Learning; 2011.

[28] Liou M-S. A sequel to AUSM, Part II: AUSM$^+$-up for all speeds. J Comput Phys 2006;214(1):137–70. http://dx.doi.org/10.1016/j.jcp.2005.09.020.

[29] Harten A. High resolution schemes for hyperbolic conservation laws. J Comput Phys 1983;49(3):357–93. http://dx.doi.org/10.1016/0021-9991(83)90136-5.

[30] Ó Conaire M, Curran HJ, Simmie JM, Pitz WJ, Westbrook CK. A comprehensive modeling study of hydrogen oxidation. Int J Chem Kinet 2004;36(11):603–22. http://dx.doi.org/10.1002/kin.20036.

[31] Girimaji S. Assumed β-pdf model for turbulent mixing: Validation and extension to multiple scalar mixing. Combust Sci Technol 1991;78(4–6):177–96. http://dx.doi.org/10.1080/00102209108951748.

[32] Baurle RA, Alexopoulos G, Hassan HA. Assumed joint probability density function approach for supersonic turbulent combustion. J Propuls Power 1994;10(4):473–84. http://dx.doi.org/10.2514/3.23797.

[33] Gerlinger P. Investigation of an assumed pdf approach for finite-rate chemistry. Combust Sci Technol 2003;175(5):841–72. http://dx.doi.org/10.1080/00102200302410.

[34] Gerlinger P, Noll B, Aigner M. Assumed PDF modelling and PDF structure investigation using finite-rate chemistry. Prog Comput Fluid Dyn Int J 2005;5(6):334–44. http://dx.doi.org/10.1504/PCFD.2005.007066.

[35] Lockwood F, Naguib A. The prediction of the fluctuations in the properties of free, round-jet, turbulent, diffusion flames. Combust Flame 1975;24:109–24. http://dx.doi.org/10.1016/0010-2180(75)90133-9.

[36] Girimaji S. A simple recipe for modeling reaction-rate in flows with turbulent-combustion. In: 22nd Fluid Dynamics, Plasma Dynamics and Lasers Conference. AIAA Paper 1991-1792, 1991, http://dx.doi.org/10.2514/6.1991-1792.

[37] Wilcox DC. Reassessment of the scale-determining equation for advanced turbulence models. AIAA J 1988;26(11):1299–310. http://dx.doi.org/10.2514/3.10041.

[38] Wilcox DC. Formulation of the k-ω turbulence model revisited. AIAA J 2008;46(11):2823–38. http://dx.doi.org/10.2514/1.36541.

[39] Gritskevich MS, Garbaruk AV, Schütze J, Menter FR. Development of DDES and IDDES formulations for the k-ω shear stress transport model. Flow Turbul Combust 2012;88(3):431–49. http://dx.doi.org/10.1007/s10494-011-9378-4.

[40] Friess C, Davidson L. A formulation of PANS capable of mimicking IDDES. Int J Heat Fluid Flow 2020;86:108666. http://dx.doi.org/10.1016/j.ijheatfluidflow.2020.108666.

[41] Probst A, Reuß S. Scale-resolving simulations of wall-bounded flows with an unstructured compressible flow solver. In: Girimaji S, Haase W, Peng S-H, Schwamborn D, editors. Progress in hybrid RANS-LES modelling. Cham: Springer International Publishing; 2015, p. 481–91. http://dx.doi.org/10.1007/978-3-319-15141-0_39.

[42] Mockett C, Fuchs M, Thiele F. Progress in DES for wall-modelled LES of complex internal flows. Comput & Fluids 2012;65:44–55. http://dx.doi.org/10.1016/j.compfluid.2012.03.014.

[43] He C, Liu Y, Yavuzkurt S. A dynamic delayed detached-eddy simulation model for turbulent flows. Comput & Fluids 2017;146:174–89. http://dx.doi.org/10.1016/j.compfluid.2017.01.018.

[44] Yoshizawa A. Statistical theory for compressible turbulent shear flows, with the application to subgrid modeling. Phys Fluids 1986;29(7):2152–64. http://dx.doi.org/10.1063/1.865552.

[45] Speziale CG, Erlebacher G, Zang TA, Hussaini MY. The subgrid-scale modeling of compressible turbulence. Phys Fluids 1988;31(4):940–2. http://dx.doi.org/10.1063/1.866778.

[46] Kok JC, Dol HS, Oskam B, van der Ven H. Extra-large eddy simulation of massively separated flows. In: 42nd AIAA Aerospace Sciences Meeting and Exhibit. AIAA Paper 2004-264, American Institute of Aeronautics and Astronautics; 2004, http://dx.doi.org/10.2514/6.2004-264.

[47] Yan J, Mockett C, Thiele F. Investigation of alternative length scale substitutions in detached-eddy simulation. Flow Turbul Combust 2005;74:85–102. http://dx.doi.org/10.1007/s10494-005-6916-y.

[48] Comte-Bellot G, Corrsin S. Simple Eulerian time correlation of full-and narrow-band velocity signals in grid-generated, 'isotropic' turbulence. J Fluid Mech 1971;48(2):273–337. http://dx.doi.org/10.1017/S0022112071001599.

[49] Wray A. Direct numerical simulation of decaying turbulence in a triply periodic box at 512^3 resolution. 1997, URL https://torroja.dmt.upm.es/turbdata/agard/, Unpublished DNS data available at AGARD database.

[50] Bunge U, Mockett C, Thiele F. Guidelines for implementing detached-eddy simulation using different models. Aerosp Sci Technol 2007;11(5):376–85. http://dx.doi.org/10.1016/j.ast.2007.02.001.

[51] Lee M, Moser RD. Direct numerical simulation of turbulent channel flow up to $Re_\tau \approx 5200$. J Fluid Mech 2015;774:395–415. http://dx.doi.org/10.1017/jfm.2015.268.

[52] Davidson L. Large eddy simulations: How to evaluate resolution. Int J Heat Fluid Flow 2009;30(5):1016–25. http://dx.doi.org/10.1016/j.ijheatfluidflow.2009.06.006.

[53] Piomelli U, Balaras E, Pasinato H, Squires KD, Spalart PR. The inner–outer layer interface in large-eddy simulations with wall-layer models. Int J Heat Fluid Flow 2003;24(4):538–50. http://dx.doi.org/10.1016/S0142-727X(03)00048-1.

[54] Pope SB. Turbulent flows. Cambridge University Press; 2001.

[55] Driver DM, Seegmiller HL. Features of a reattaching turbulent shear layer in divergent channel flow. AIAA J 1985;23(2):163–71. http://dx.doi.org/10.2514/3.8890.

[56] Driver DM, Seegmiller HL, Marvin JG. Time-dependent behavior of a reattaching shear layer. AIAA J 1987;25(7):914–9. http://dx.doi.org/10.2514/3.9722.

[57] Wang L, Hu R, Li L, Fu S. Detached-eddy simulations for active flow control. AIAA J 2018;56(4):1447–62. http://dx.doi.org/10.2514/1.J055891.

[58] Shur ML, Spalart PR, Strelets MK, Travin AK. An enhanced version of DES with rapid transition from RANS to LES in separated flows. Flow Turbul Combust 2015;95(4):709–37. http://dx.doi.org/10.1007/s10494-015-9618-0.

[59] Marshall W, Pal S, Woodward R, Santoro R. Benchmark wall heat flux data for a GO_2/GH_2 single element combustor. In: 41st AIAA/ASME/SAE/ASEE Joint Propulsion Conference & Exhibit. AIAA Paper 2005-3572, American Institute of Aeronautics and Astronautics; 2005, http://dx.doi.org/10.2514/6.2005-3572.

[60] Pal S, Marshall W, Woodward R, Santoro R. Wall heat flux measurements for a uni-element GO_2/GH_2 shear coaxial injector. In: Third International Workshop on Rocket Combustion Modeling. 2006.

[61] Tucker PK, Menon S, Merkle CL, Oefelein JC, Yang V. An approach to improved credibility of CFD calculations for rocket injector design. In: 43rd AIAA/ASME/SAE/ASEE Joint Propulsion Conference & Exhibit. AIAA Paper 2007-5572, American Institute of Aeronautics and Astronautics; 2007, http://dx.doi.org/10.2514/6.2007-5572.

[62] Tucker PK, Menon S, Merkle CL, Oeflein JC, Yang V. Validation of high-fidelity CFD simulations for rocket injector design. In: 44th AIAA/ASME/SAE/ASEE Joint Propulsion Conference & Exhibit. AIAA Paper 2008-5226, American Institute of Aeronautics and Astronautics; 2008, http://dx.doi.org/10.2514/6.2008-5226.

[63] Ivancic B, Riedmann H, Frey M, Knab O, Karl S, Hannemann K. Investigation of different modeling approaches for computational fluid dynamics simulation of high-pressure rocket combustors. Prog Propuls Phys 2016;8:95–116. http://dx.doi.org/10.1051/eucass/201608095.

[64] Huo H, Yang V. Large-eddy simulation of supercritical combustion: Model validation against gaseous H2-O2 injector. J Propuls Power 2017;33(5):1272–84. http://dx.doi.org/10.2514/1.B36368.

[65] Ma PC, Wu H, Ihme M, Hickey J-P. A flamelet model with heat-loss effects for predicting wall-heat transfer in rocket engines. In: 53rd AIAA/SAE/ASEE Joint Propulsion Conference. AIAA Paper 2017-4856, American Institute of Aeronautics and Astronautics; 2017, http://dx.doi.org/10.2514/6.2017-4856.

[66] Yao W, Li B. Application of dynamic zone flamelet model to a GH_2/GO_2 rocket combustor. In: AIAA Propulsion and Energy 2019 Forum. 2019, http://dx.doi.org/10.2514/6.2019-3868.

[67] Masquelet M, Menon S. Large-eddy simulation of flame-turbulence interactions in a shear coaxial injector. J Propuls Power 2010;26(5):924–35. http://dx.doi.org/10.2514/1.48023.

[68] Kindler M. Verbrennungssimulation in instationären kompressiblen strömungen (Ph.D. thesis), University of Stuttgart; 2014, http://dx.doi.org/10.18419/opus-3952.